Impact of Picoliter Droplets on Superhydrophobic Surfaces with Ultralow Spreading Ratios
P. S. Brown, A. Berson, E. L. Talbot, T. J. Wood, W. C. E. Schofield, C. D. Bain, and J. P. S. Badyal
Langmuir 27 (2011) 13897– 13903.

IMPACT OF PICOLITRE DROPLETS ON SUPERHYDROPHOBIC SURFACES WITH ULTRA-LOW SPREADING RATIOS

P. S. Brown, A. Berson, E. L. Talbot, T. J. Wood, W. C. E. Schofield, C. D. Bain[†], and J. P. S. Badyal[†*]

Department of Chemistry
Science Laboratories
Durham University
Durham DH1 3LE
England, UK

* Corresponding author.

[†] JPSB and CDB have made equal contributions to this piece of work.

TABLE OF CONTENTS GRAPHIC

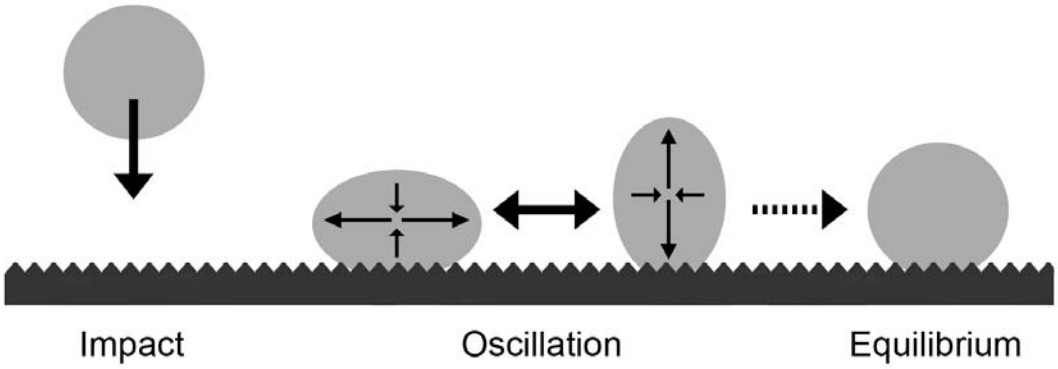

ABSTRACT

The impact of picolitre sized water droplets upon superhydrophobic CF_4 plasma fluorinated polybutadiene surfaces is investigated with high-speed imaging. Variation of the surface topography by plasmachemical modification enables the dynamics of wetting to be precisely controlled. Final spreading ratios as low as 0.63 can be achieved. Comparison of the maximum spreading ratio and droplet oscillation frequencies with models described in the literature shows that both are found to be much lower than theoretically predicted.

1. INTRODUCTION

Droplet impact upon solid surfaces is a widespread phenomenon and has been investigated for over a century.[1] Important technological applications include: rapid cooling,[2,3,4] delayed freezing,[5,6,7,8] crop spraying,[9] and inkjet printing. In recent years, work has been carried out to assess the feasibility of inkjet printing technology in manufacturing processes. In the case of the latter, the resolution of impact is critical for patterning applications such as: microelectronics,[10,11,12,13] pharmaceutical dosing or screening,[14,15,16] tissue engineering, [17,18] and optics.[19,20]

Typically, the impact of a droplet onto a solid surface can be divided into four regimes.[21] The first involves the initial impact and is largely dependent upon the fluid properties of the drop. During the second phase, the droplet spreads to a maximum diameter on the surface, which is determined by a balance between the inertia of the drop (governed by its diameter, velocity, viscosity, and density) and surface tension forces. The third phase entails the dissipation of the droplet inertia, as seen by oscillations in the height, width, and contact area diameter of the drop on the surface. This phase is highly dependent upon the fluid and substrate surface energies which determine the static and dynamic contact angles. The final stage encompasses the relaxation of the drop towards its equilibrium diameter.

Whilst liquid properties are important during drop impact,[22] there exists strong evidence suggesting that surface properties not only affect the final static diameter of the droplet, but other key aspects of the surface impact.[21,23,24,25,26,27,28]

For topographically complex superhydrophobic surfaces, the impacting droplet can either penetrate into the surface fine structure, or become suspended on the asperities creating air pockets underneath giving a composite solid-air interface. These are respectively the Wenzel[29] and Cassie-Baxter[30] states. Droplet impact onto rough superhydrophobic surfaces usually results in bouncing[31,32] or splashing.[33,34,35,36,37] The situation is further complicated in that the inertia may be sufficient to impale the droplet onto surface features forcing a Wenzel configuration.[38,39] Few droplet impact

studies as a function of surface roughness are reported[37,40,41], because surface roughness is difficult to define and control.[42]

In this study, impact of picolitre sized droplets is investigated across a range of surface roughness values. The superhydrophobic surfaces were prepared by plasmachemical fluorination of polybutadiene films yielding sessile drop water contact angle values exceeding 170°, with negligible contact angle hysteresis.[43,44] The surface roughness was varied whilst maintaining a constant surface chemistry. The influence of the substrate on the static and dynamic spreading ratio as well as on droplet oscillations has been investigated and the results compared with models from the literature.

2. EXPERIMENTAL

2.1 Sample Preparation

Polybutadiene (Sigma-Aldrich Inc., M_w = 420,000, 36% cis 1,4 addition, 55% trans 1,4 addition, 9% 1,2 addition) dissolved in toluene (BDH, +99.5% purity) at a concentration of 5% (w/w) was spin coated onto polished silicon (100) wafers (Silicon Valley Microelectronics Inc.) using a photoresist spinner (Cammax Precima) operating at 3000 rpm. These polymer films were subsequently annealed at 90 °C under vacuum for 60 min to remove entrapped solvent.

Plasmachemical fluorination was carried out in a cylindrical glass reactor (5 cm diameter, 470 cm^3 volume) connected to a two stage rotary pump via a liquid nitrogen cold trap with a base pressure of 4 x 10^{-3} mbar and a leak rate better than 6 x 10^{-9} mol s^{-1}. An L-C matching unit was used to minimise the standing wave ratio (SWR) for the power transmitted from a 13.56 MHz radio frequency generator to a copper coil externally wound around the glass reactor. Prior to each plasma treatment, the chamber was scrubbed with detergent, rinsed in propan-2-ol, and further cleaned using a 50 W air plasma for 30 min. A piece of polybutadiene coated substrate was then placed into the centre of the reactor, followed by evacuation to base pressure. Next, CF_4 gas (99.7% purity, Air Products) was admitted into the system via a needle valve at a pressure of 0.2 mbar, and the electrical discharge ignited.

Upon completion of surface functionalisation, the gas feed was turned off and the chamber vented to atmosphere.

2.2 Sample Characterisation

A VG ESCALAB spectrometer equipped with an unmonochromatised Mg K_α X-ray source (1253.6 eV) and a concentric hemispherical analyser (CAE mode pass energy = 20 eV) was used for X-ray photoelectron spectroscopy (XPS) analysis. The XPS spectra were referenced to the C(1s) peak at 285.0 eV and fitted with a linear background and equal full-width-at-half maximum (FWHM) Gaussian components.[45] Elemental compositions were calculated using sensitivity factors derived from chemical standards, F(1s): O(1s): C(1s) equals 0.27: 0.40: 1.00.

Contact angle analysis was carried out with a video capture system (ASE Products, VCA2500XE) using 1.0 µL droplets of de-ionised water.

AFM images were acquired using a Digital Instruments Nanoscope III scanning probe microscope. Damage to the tip and sample surface was minimised by employing Tapping Mode AFM. Root-mean-square (RMS) roughness values were calculated over 50 µm x 50 µm scan areas.

2.3 Drop Impact and Imaging

The inkjet nozzle (Horizon Instruments Ltd., MicroFab MJ-ABP-01) was a piezo-type nozzle with a diameter of 30 µm. Water droplets of 30 µm diameter were generating using a drive voltage of 9 V to provide a pulse waveform comprising a rise time of 2 µs, a dwell width of 15 µs, a fall time of 2 µs, an echo of 45 µs, and a final rise time of 2 µs. The distance between the nozzle tip and the substrate surface was set at 0.4 mm. Impact speeds were typically between 0.8 and 1.2 m s^{-1}. The temperature of the nozzle was 30 °C. A high speed camera (Photron Europe Ltd., FASTCAM APX RS) in conjunction with a microscopic objective lens (Nikon U.K. Ltd., M Plan) with a magnification of 20x were used to observe the droplet. A back lighting system (Thorlabs Ltd., HPLS-30-02) was used for the illumination source. 90000 frames per second were achieved, to give an image every 11 µs. The shutter speed was set to 1 µs. Each frame consisted of 128 x 96 pixels, with the the pixel size equal to 0.73 µm. The jetting driver was triggered by the camera.

Droplet impact can be described using the following three dimensionless numbers.[46,47] The Weber (*We*) number:

$$We = \frac{\rho D_0 U_0^2}{\sigma} \quad (1)$$

the Ohnesorge (*Oh*) number:

$$Oh = \frac{\mu}{\sqrt{D_0 \sigma \rho}} \quad (2)$$

and the Reynolds (*Re*) number:

$$Re = \frac{\rho D_0 U_0}{\mu} = \frac{\sqrt{We}}{Oh} \quad (3)$$

D_0 and U_0 are the diameter and velocity before impact (both of which can be varied experimentally). ρ, σ, and μ are the density, surface tension, and viscosity of the fluid.

Undesirable droplet behaviour, such as bouncing or splashing, was supressed by fine-tuning of these dimensionless parameters, Equation 1. Throughout this study, picolitre water droplets with *We* = 0.3 – 0.6, *Oh* = 0.02, and *Re* = 25 – 40 were utilised.

3. RESULTS

3.1 Superhydrophobic Surfaces

The XPS elemental composition of spin coated polybutadiene was 86% C, 14% O, and 0% F. Following CF_4 plasma fluorination, a constant F:C ratio across a range of electrical discharge powers was measured,[43] Figure 1. Therefore, any variation in the droplet impact regime can primarily be attributed to a change in surface topography.

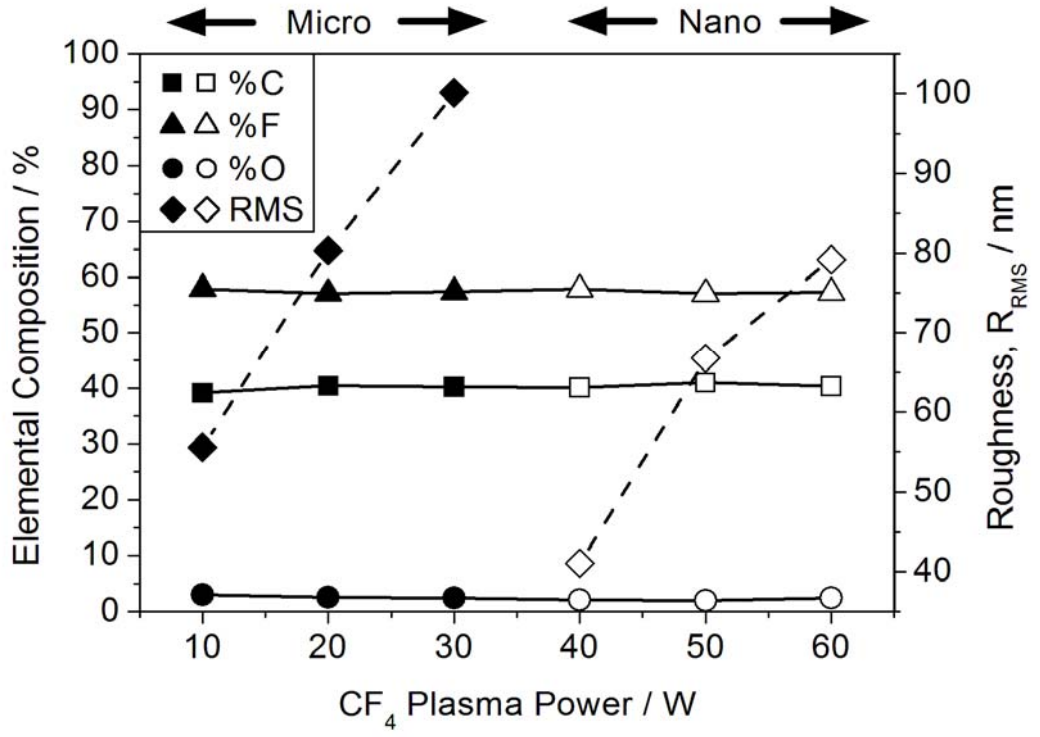

Figure 1. XPS and AFM RMS roughness analysis following 5 min CF_4 plasma fluorination of polybutadiene surfaces as a function of power. The lines are guides to the eye. Closed symbols denote microscale features, and open symbols denote nanoscale features. Error values: Elemental Composition = ± 2%; Roughness, R_{RMS} = ± 5 nm.

The surface roughness of the freshly prepared polybutadiene surfaces was measured to be R_{RMS} = 7 ± 1 nm. CF_4 plasma fluorination gave rise to two distinct regimes of surface topography as observed by AFM, Figures 1 and 2. Large scale (micro) undulating features, observed at low powers, which are replaced by finer scale (nano) roughness at higher powers.[43] Longer treatment times can result in a composite surface exhibiting two roughness length scales.

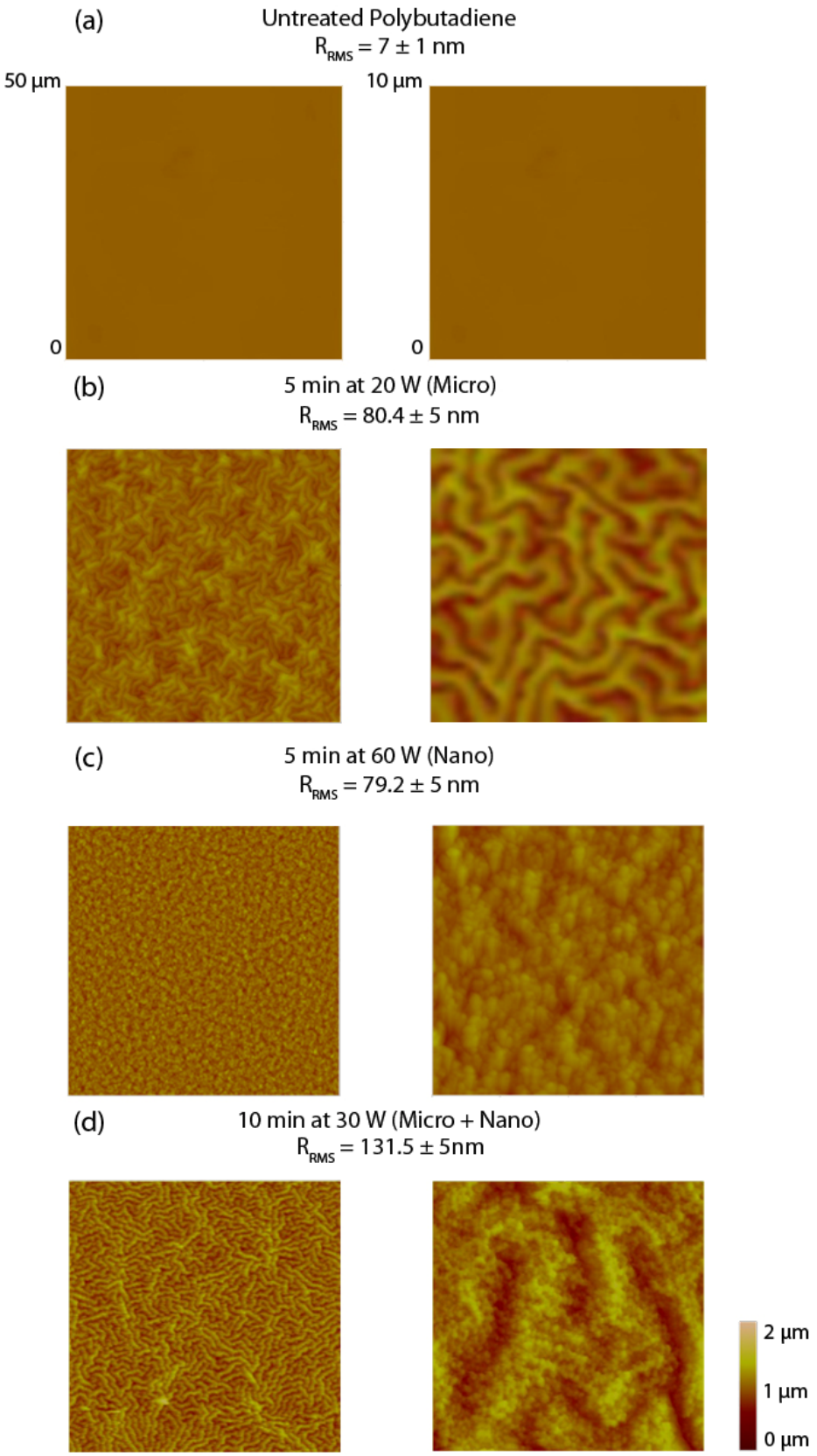

Figure 2. AFM height images of the two different surface topographies for CF_4 plasma fluorinated polybutadiene surfaces with similar RMS roughness values yet different distribution of asperities: (a) untreated polybutadiene; (b) microscale features; (c) nanoscale features; and (d) hierarchical surface.

Microlitre droplets placed onto these CF_4 plasma fluorinated polybutadiene surfaces yield contact angles ranging from 140° to 174°, Figure 3. With increasing surface roughness, the height of the asperities becomes sufficient to support a composite solid-air interface and the droplet behaviour corresponds to the Cassie-Baxter state.[30] This state is reflected in larger water contact angle values in conjunction with smaller contact angle hysteresis (θ_{adv} - θ_{rec}), Figure 3. It is worth noting that both the micro- and nanoscale topography data sit on the same equilibrium contact angle and contact angle hysteresis trend lines for R_{RMS} > 60 nm.

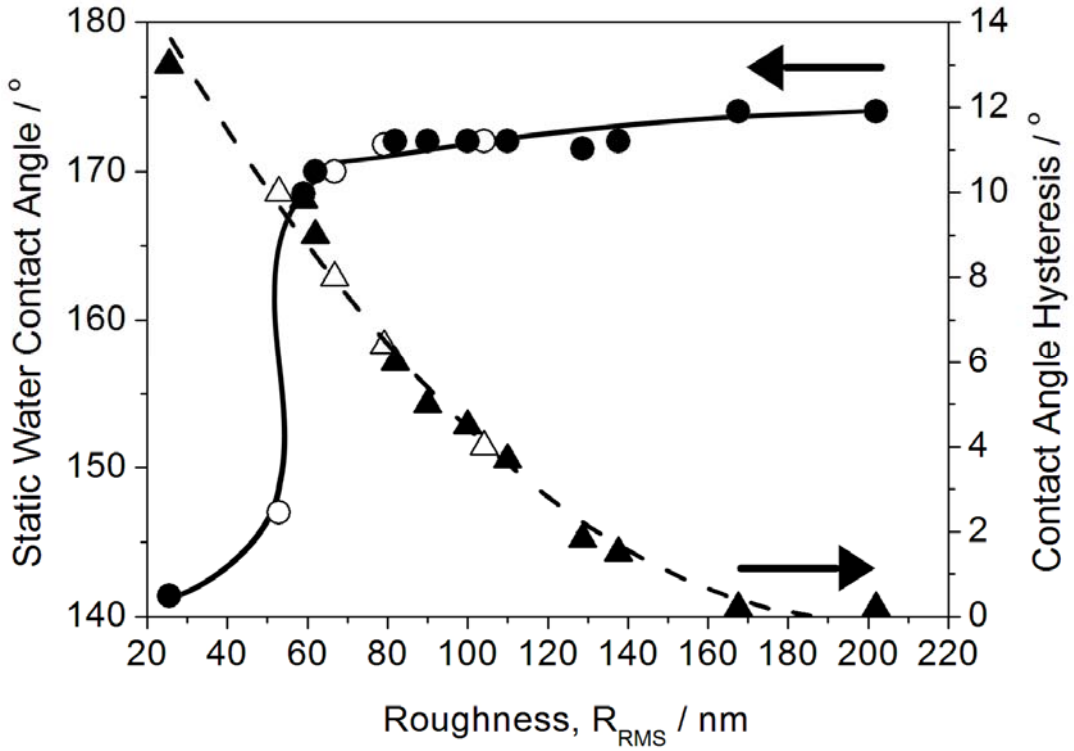

Figure 3. Static water contact angle and contact angle hysteresis values for 1.0 µL water drops placed onto CF_4 plasma fluorinated polybutadiene as a function of surface roughness. The lines are guides to the eye. Closed symbols denote microscale features, and open symbols denote nanoscale features. Error values: Static Water Contact Angle = ± 5°; Contact Angle Hysteresis ± 0.5°; Roughness, R_{RMS} = ± 5 nm.

3.2 Picolitre Droplet Impact

High-speed photography of picolitre droplets striking these superhydrophobic surfaces without bouncing or splashing shows that, following initial impact, the

droplet spreads outwards to a maximum diameter on the surface, Figure 4. Upon reaching this diameter, any excess energy will cause oscillations of the height, width, and contact line of the droplet about their static positions. The fluctuation in droplet height / width is pronounced, but the change in the contact area diameter is much more subtle. The droplet eventually comes to rest at its static position when its inertia is fully expended.

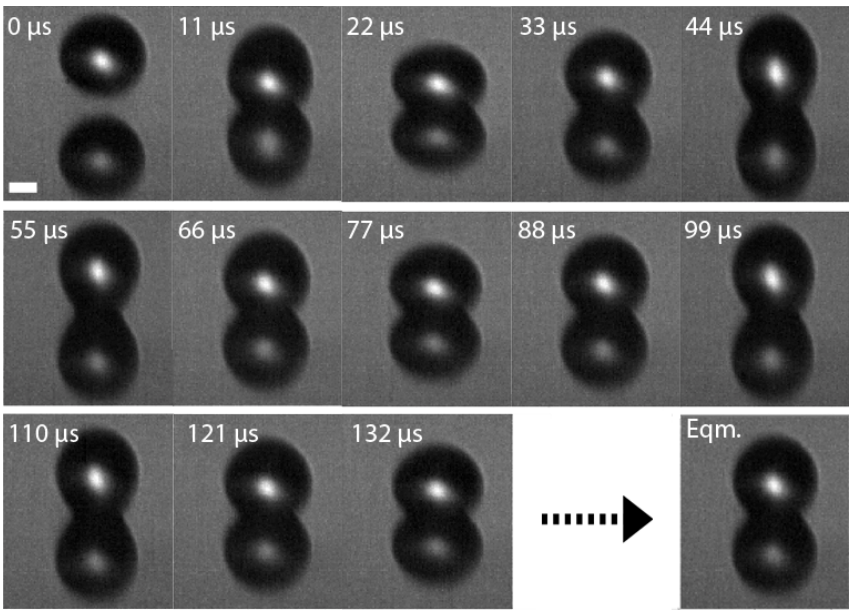

Figure 4. Typical High speed video images of a picolitre size water droplet striking a superhydrophobic CF_4 plasma fluorinated polybutadiene surface (including droplet reflection - lower image). White scale bar = 10 µm.

The higher contact angle values observed for microlitre versus picolitre water droplets resting on CF_4 plasma fluorinated polybutadiene surfaces are closer to those expected for a Wenzel state of wetting, Figure 5. Furthermore, in the case of the picolitre size droplets for comparable surface roughness values, they display larger contact angles for the nanoscale surface topography. Whilst picolitre droplets striking surfaces with roughness values exceeding R_{RMS} = 140 nm bounce, Figure 5.

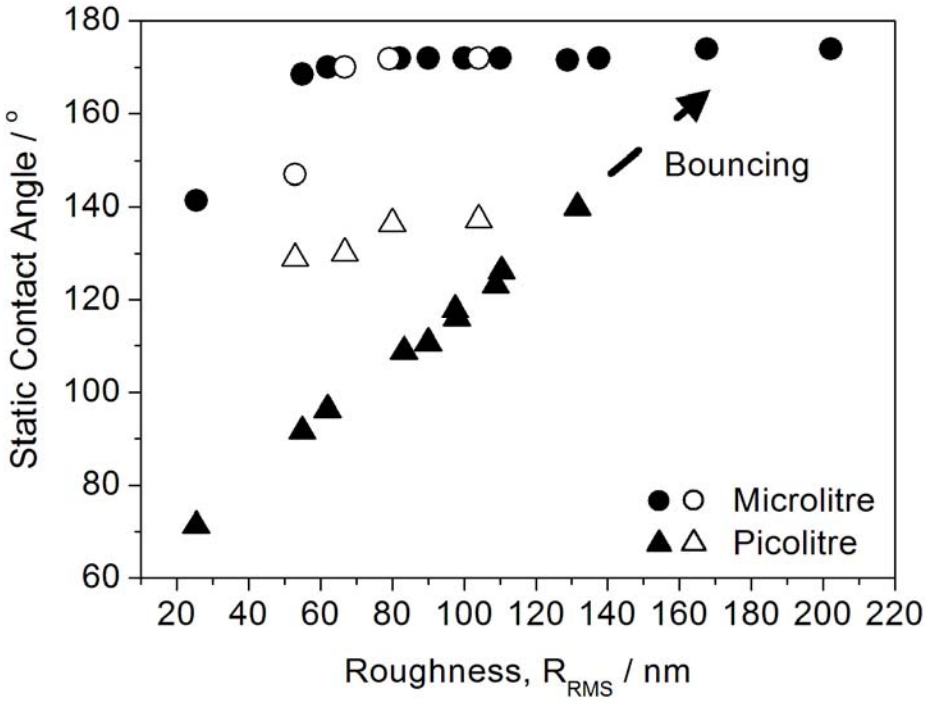

Figure 5. Static and equilibrium contact angles of microlitre and picolitre water droplets respectively on CF_4 plasma fluorinated polybutadiene as a function of surface roughness. Closed symbols denote microscale features, and open symbols denote nanoscale features. Error values: Static Water Contact Angle = ± 5°; Roughness, R_{RMS} = ± 5 nm.

The maximum spreading ratio is calculated as the maximum spread of the contact area across the surface divided by the initial diameter of the droplet. Numerous attempts have been made to model the maximum spreading ratio. The Pasandideh-Fard model[48] assumes the droplet is thin and the contact angle is low, which is not valid for superhydrophobic surfaces. A modified model by Son[27] relaxes these assumptions but violates volume conservation. The following analysis is based on the model by Attané.[49]

Attané neglects the initial kinetic energy of the droplet and viscous dissipation within the droplet which is reasonable when both *We* and *Oh* are small. At maximum spreading, all the surface energy of the droplet before impact is equal to the surface energy of the sessile droplet:

$$\sigma\pi D_0^2 = \sigma\left[A - \pi\left(\frac{D_{\max}}{2}\right)^2 \frac{\left(\sigma_{sv} - \sigma_{sl}\right)}{\sigma}\right] \qquad (4)$$

where σ is the liquid surface tension, σ_{sv} is the surface free energy of the solid-vapour interface, σ_{sl} is the surface free energy of the solid-liquid

interface (both per unit geometrical area), A is the area of the air-water interface, D_0 is the initial droplet diameter and D_{max} is the maximum spreading diameter. Young's equation allows the elimination of the solid surface free energies to give:

$$\sigma\pi D_0^2 = \sigma\left[A - \pi\left(\frac{D_{\max}}{2}\right)^2 \cos\theta_{eq}\right], \tag{5}$$

where θ_{eq} is the equilibrium contact angle. Assuming that the air-water interface is a spherical cap and that volume is conserved, Equation 5 can be rewritten as:

$$\frac{1}{3}\left[2\frac{h^2}{{D_0}^2} + \frac{D_0}{h} - \left(\frac{D_0}{h} - \frac{h^2}{{D_0}^2}\right)\cos\theta_{eq}\right] = 1, \tag{6}$$

where h is the height of the spherical cap. The maximum spreading ratio is obtained from the height as follows:

$$\frac{D_{\max}}{D_0} = 2\left[\frac{1}{3}\left(\frac{D_0}{h} - \frac{h^2}{{D_0}^2}\right)\right]^{1/2}. \tag{7}$$

Equations 6 and 7 provide an upper limit for the maximum spreading ratio as they assume there is no dissipation. The practical problem is concerned with knowing the value of θ_{eq}. We assume here that θ_{eq} is the same as the static contact angle, θ, when the droplet motion has ceased. A lower limit to D_{max} is given by the static spreading ratio:

$$\frac{D_s}{D_0} = 2\left[\frac{\sin^3\theta}{4 - 6\cos\theta + 2\cos^3\theta}\right]^{1/3}. \tag{8}$$

Experimental maximum spreading ratios are compared to the results of Equations 7 and 8 in Figure 6.

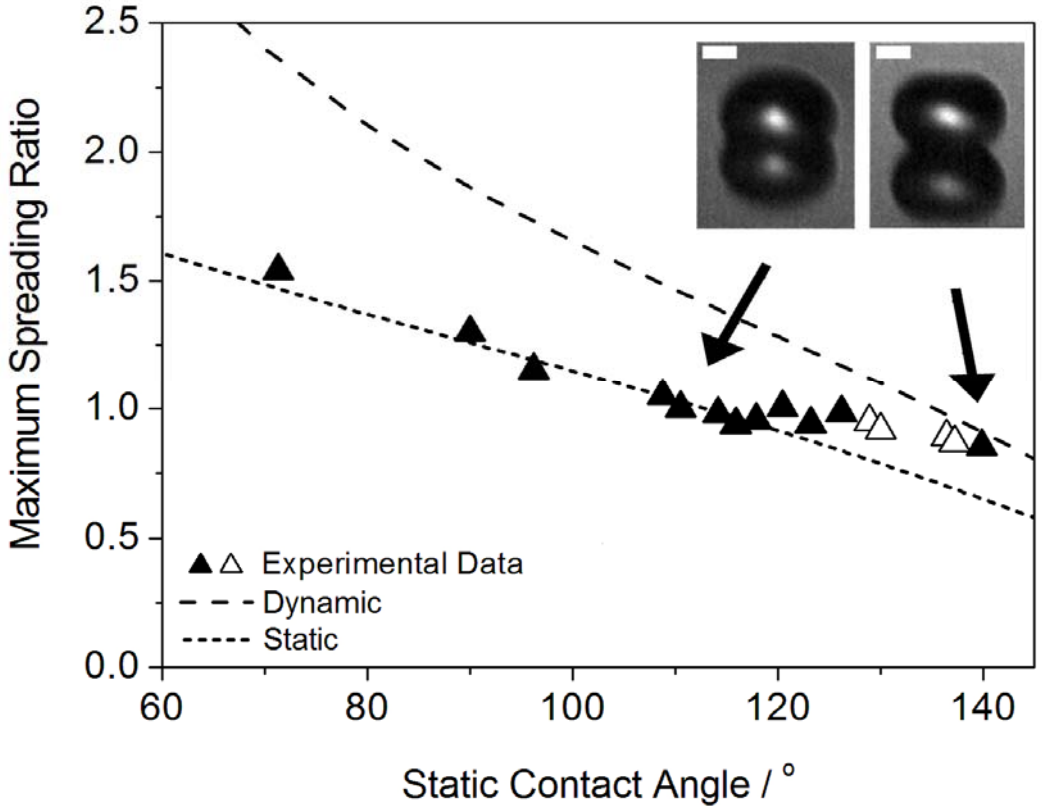

Figure 6. Maximum spreading ratios (D_{max}/D_0) as a function of static contact angle for picolitre sized water droplets. Experimental data is compared with the two limiting cases of maximum dynamic spreading (Equation 7) and static contact angle (Equation 8). Closed symbols denote microscale features, and open symbols denote nanoscale features. Inset: Images of droplets during maximum spreading on microscale features. White scale bar = 10 μm. Error values: Spreading Ratio = ± 0.05; Static Contact Angle = ± 5°.

The oscillation of the contact diameter for picolitre droplets after impact was fitted to the damped oscillation equation: [50]

$$y = a_0 + a_1 e^{-a_2 t} \cos(a_3 t + a_4) \,, \qquad (9)$$

where a_0 - a_4 are fitting parameters, t is time, and y is droplet height, width, or contact area diameter. The first oscillation of the droplet was discarded because it is influenced by internal flows arising from the droplet impact.[21] Beyond the first oscillation, a good fit to Equation 9 was obtained, Figure 7.

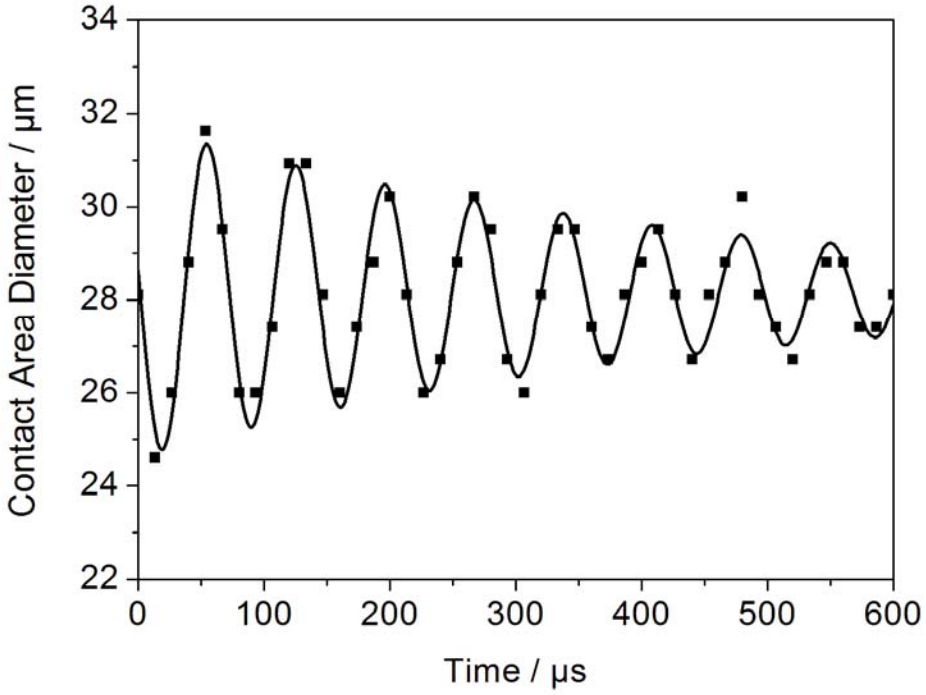

Figure 7. Typical damped oscillating curve (Equation 9) fitted to the experimental data for picolitre water droplet fluctuation following impact.

Figure 8 plots the oscillation frequency and half-life (= ln2/a_2) as a function of static contact angle of picolitre droplets. The higher the static water contact angles, the lower the frequency of oscillation and the longer the half-life.

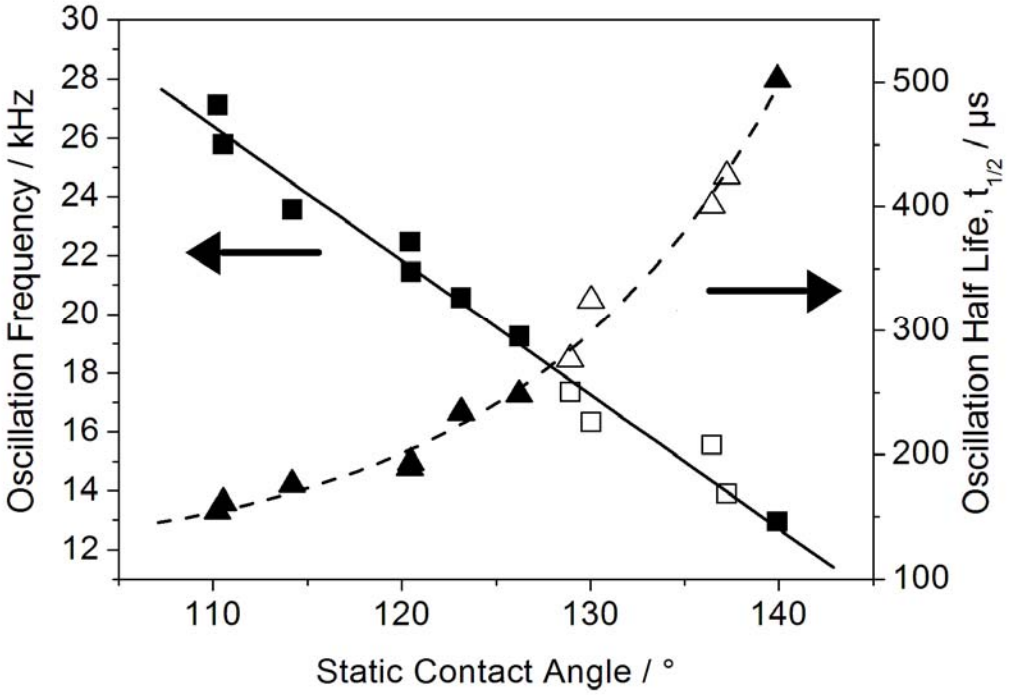

Figure 8. Frequency and half-life of the oscillation in height, contact area and diameter of picolitre sized water droplets following surface impact as a function of measured static contact angle. Closed symbols denote microscale features, and open symbols denote nanoscale features. Error values: Oscillation Frequency = ± 0.5 kHz; Oscillation Half Life = ± 20 µs; Static Contact Angle = ± 5°.

The static spreading ratio (D_{eqm}/D_0) is found to decrease with increasing surface roughness, Figure 9. However, two distinct regimes are evident which correspond to the two different types of surface roughness features (micro or nano), Figure 2. Where the two regimes meet corresponds to droplet impact on a surface featuring both roughness length scales (micro and nano).

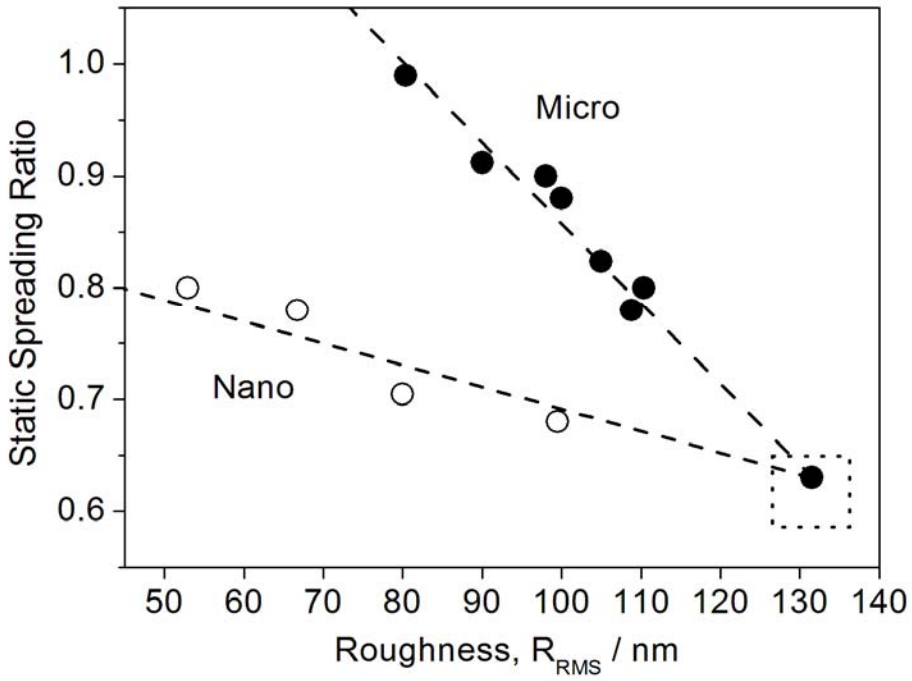

Figure 9. Static spreading ratio (D_{eqm}/D_0) of picolitre sized water droplets as a function of RMS surface roughness. Closed symbols denote microscale features, and open symbols denote nanoscale features. Highlighted data points denote composite surface. Error values: Static Spreading Ratio = ± 0.05; Roughness, R_{RMS} = ± 5nm.

4. DISCUSSION

Plasmachemical fluorination of polybutadiene yields superhydrophobic surfaces[43,44] as predicted by previously derived structure-behaviour relationships.[51] The high level of sp^2 carbon centres leads to a large F:C ratio as a consequence of atomic fluorine addition to carbon-carbon double bonds being the major reaction pathway as well as straight forward hydrogen substitution.[51] Concurrently there is phase induced surface roughening. Polybutadiene films consist of crystalline and amorphous regions.[52] Large undulating features, arising due to the difference in plasma etching rates of crystalline and amorphous polymer,[53,54,55] give way to finer scale roughness features at higher plasma powers.

Static contact angle measurements show that a surface roughness of R_{RMS} = 60 nm is sufficient to promote a hydrophobic state for microlitre size water droplets, Figure 3. For a truly superhydrophobic state, a small contact

angle hysteresis is usually required (2° or less);[56,57,58] this is achieved for microlitre size droplets on plasma fluorinated substrates with a surface roughness value of a least R_{RMS} = 120 nm, Figure 3.

Experiments were conducted at low Weber and Ohnesorge numbers where the spreading model of Attané, based on conservation of surface free energy, might be expected to hold. For final (static) contact angles $\theta \leq 110°$, the maximum spreading ratio for picolitre drops coincides with the static ratio: in other words, the contact line does not retract. The maximum spreading ratio is much less than that predicted by the Attané model. There are two plausible explanations for this discrepancy, both of which may act simultaneously. First, the excess surface free energy is dissipated in the motion of the contact line across the surface. Evidence to support this explanation is that these droplets do not show observable oscillations from the excess energy of the droplet. Second, it is not appropriate to use the static contact angle in place of the equilibrium contact angle in Equation 6. If a surface exhibits large contact angle hysteresis then, provided that the contact angle at maximum spreading is greater than the receding angle, the contact line will not retract. The equilibrium contact angle on surfaces with hysteresis lies between the maximum advancing and minimum receding contact angles. Evidence to support this view is that static contact angles of 60–100° reported in Figure 6 are low for water on flat fluorinated surfaces. If $\theta_{eq} > \theta$, the discrepancy between the theoretical prediction and the experimental data is reduced.

For static contact angles $\theta \geq 110°$, the maximum spreading ratio is larger than the static one (the contact line recedes) and oscillations are observed in the shape of the droplet demonstrating that spreading does not dissipate all the excess surface energy. The experimental maximum spreading ratios tend towards the Attané prediction as the static contact angle increases. However, we note that the assumption of a spherical cap does not hold for drops with static contact angles greater than 120° (see Figure 6, inset). Instead, the droplet flattens to minimise unfavourable spreading, thus reducing the maximum spreading ratio measured.

As noted above, impacting droplets with static contact angles > 110° undergo damped oscillations after spreading. There are very few models or experimental data in the literature on the oscillations of sessile droplets that

cover a range of contact angles as wide as explored here. Strani and Sabetta[59,60] dervived an analytical model for the free oscillations of spherical droplets sitting in a solid, spherical cup with a pinned contact line. These models are close to our experimental situation with the exception that the solid is flat, not cupped. The Strani and Sabetta model predicts lower oscillation frequencies for higher contact angles, in agreements with our experimental data. However, theoretical results overestimate the experimental oscillation frequencies by a factor of approximately two. This disparity is most likely due to contact line motion. In the model, the contact line is pinned whereas, in the experimental data, the droplet dynamics include a moving contact line. It is also possible that the rough surfaces inhibit contact line motion,[61] meaning the droplet oscillates at a lower frequency than that expected.

A useful way to describe the deposition of a droplet onto a surface is to use a spreading ratio, which is calculated by dividing the diameter of the contact area by the diameter of the droplet during free flight. For inkjet applications, a small spreading ratio is highly desirable because it minimises the spread of the droplet across the surface leading to high definition printing. Previous studies of substrate wettability in regimes relevant for inkjet printing have reported equilibrium spreading ratios of 1.0 or higher.[23,62] The dotted line in Figure 6 shows that for contact angles > 110°, the spreading ratio is less than unity. The minimum value of the spreading ratio that was achieved in this study was 0.63 (Figure 9), which is believed to be the smallest spreading ratio reported for picolitre droplets. This spreading ratio was achieved on a composite surface with roughness on two length scales which is believed to be important for superhydrophobicity.[63] It is envisaged that such smaller contact areas could be utilised to improve the resolution of inkjet printing techniques, without the need to modify the base ink. The limitation of the current surfaces is that picolitre droplets with impact velocities typical of commercial inkjet printers tend to bounce.

By plotting static spreading ratio as a function of surface roughness, Figure 9, it is clear that two distinct regimes of roughness (micro or nano) exist with their corresponding different droplet impact behaviours, Figure 2. For microlitre drops, this regime change has no effect on the droplet

behaviour observed since the droplet is several orders of magnitude larger than the roughness features. However, in the case of picolitre droplets, the contact area diameter is only an order of magnitude larger than the asperities, making picolitre droplet behaviour more dependent upon the surface topography. These spreading characteristics are influenced by the precise nature of the surface roughness.

5. CONCLUSIONS

The impact and spreading of picolitre droplets of water onto superhydrophobic CF_4 plasma fluorinated polybutadiene surfaces is strongly influenced by the length-scale of surface topography (for similar roughness values). Large differences are observed between the behaviour of microlitre and picolitre drops, implying that measurements made with conventional contact angle instruments are unlikely to be good predictors of inkjet behaviour. Impacting droplet oscillation frequency is found to decrease with increasing static contact angle providing a good qualitative agreement, albeit a poor quantitative one, with available models. Work is currently underway to apply numerical models of wetting dynamics[64] to the impact and relaxation of picolitre droplets on superhydrophobic surfaces. A static spreading ratio of 0.63 has been measured which is lower than previously reported values.

6. ACKNOWLEDGEMENTS

We would like to thank EPSRC for financial support (Grant Reference No. EP/H018913/1).

7. REFERENCES

[1] Worthington, A. M. *Proc. R. Soc. Lond.* **1876**, *25*, 261.

[2] Yao, S. C.; Choi, K. J. *Int. J. Multiphase Flow* **1987**, *13*, 639.

[3] Pasandideh-Fard, M.; Aziz, S. D.; Chandra, S.; Mostaghimi, J. *Int.J. Heat and Fluid Flow* **2001**, *22*, 201.

[4] Chen, R.-H.; Chow, L. C.; Navedo, J. E. *Int. J. Heat Mass Tran.* **2002**, *45*, 4033.

[5] Tourkine, P.; Le Merrer, M.; Quéré, D. *Langmuir* **2009**, *25*, 7214.

[6] Kulinich, S. A.; Farzaneh, M. *Langmuir* **2009**, *25*, 8854.

[7] Cao, L.; Jones, A. K.; Sikka, V. K.; Wu, J.; Gao, D. *Langmuir* **2009**, *25*, 12444.

[8] Mishchenko, L.; Hatton, B.; Bahadur, V.; Taylor, J. A.; Krupenkin, T.; Aizenberg, J. *ACS Nano* **2010**, *4*, 7699.

[9] Reichard, D. L. *Weed Technol.* **1988**, *2*, 82.

[10] Sirringhaus, H.; Kawase, T.; Friend, R. H.; Shimoda, T.; Inbasekaran, M.; Wu, W.; Woo, E. P. *Science* **2000**, *290*, 2123.

[11] Wang, J. Z.; Zheng, Z. H.; Li, H. W.; Huck, W. T. S.; Sirringhaus, H. *Nat. Mater.* **2004**, *3*, 171.

[12] Sele, C. W.; von Werne, T.; Friend, R. H.; Sirringhaus, H. *Adv. Mater.* **2005**, *17*, 997.

[13] Doggart, J.; Wu, Y.; Liu, P.; Zhu, S. *ACS Appl. Mater. Interfaces* **2010**, *2*, 2189.

[14] Barbulovic-Nad, I.; Lucente, M.; Sun, Y.; Zhang, M.; Wheeler, A. R.; Bussmann, M. *Crit. Rev. Biotechnol.* **2006**, *26*, 237.

[15] Tan, C. P.; Cipriany, R.; Lin, D. M.; Craighead, H. G. *Nano Lett.* **2010**, *10*, 719.

[16] Arrabito, G.; Pignataro, B. *Anal. Chem.* **2010**, *82*, 3104.

[17] Mironov, V.; Boland, T.; Trusk, T.; Forgacs, G.; Markwald, R. R. *Trends Biotechnol.* **2003**, *21*, 157.

[18] Xu, T.; Jin, J.; Gregory, C.; Hickman, J. J.; Boland, T. *Biomaterials* **2005**, *26*, 93.

[19] Bharathan, J.; Yang, Y. *Appl. Phys. Lett.* **1998**, *72*, 2660.

[20] Chang, S.-C.; Bharathan, J.; Yang, Y.; Helgeson, R.; Wudl, F.; Ramey, M. B.; Reynolds, J. R. *Appl. Phys. Lett.* **1998**, *73*, 2561.

[21] Rioboo, R.; Marengo, M.; Tropea, C. *Exp. Fluids* **2002**, *33*, 112.

[22] Mao, T.; Kuhn, D. C. S.; Tran, H. *AIChE J.* **1997**, *43*, 2169.

[23] Dong, H.; Carr, W. W.; Bucknall, D. G.; Morris, J. F. *AIChE J.* **2007,** *53*, 2606.

[24] Šikalo, Š.; Marengo, M.; Tropea, C.; Ganić, E. N. *Exp. Therm. Fluid Sci.* **2002**, *25*, 503.

[25] Wang, M.-J.; Lin, F.-H.; Hung, Y.-L.; Lin, S.-Y. *Langmuir* **2009**, *25*, 6772.

[26] Ukiwe, C.; Mansouri, A.; Kwok, D. Y. *J. Coll. Int. Sci.* **2005**, *285*, 760.

[27] Son, Y.; Kim, C.; Yang, D. H.; Ahn, D. J. *Langmuir* **2008**, *24*, 2900.

[28] Son, Y.; Kim, C.; *J. Non-Newtonian Fluid Mech.* **2009**, *162*, 78.

[29] Wenzel, R, N. *Ind. Eng. Chem.* **1936**, *28*, 988.

[30] Cassie, A. B. D.; Baxter, S. *Trans. Faraday Soc.* **1944**, *40*, 546.

[31] Jung, Y. C.; Bhushan, B. *Langmuir* **2008**, *24*, 6262.

[32] Brunet, P.; Lapierre, F.; Thomy, V.; Coffinier, Y.; Boukherroub, R. *Langmuir* **2008**, *24*, 11203.

[33] Tsai, P.; Pacheco, S.; Pirat, C.; Lefferts, L.; Lohse, D. *Langmuir* **2009**, *25*, 12293.

[34] Rioboo, R.; Marengo, M.; Tropea, C. *Atomization Spray* **2001**, *11*, 155.

[35] Deng, T.; Varanasi, K. K.; Hsu, M.; Bhate, N.; Keimel, C.; Stein, J.; Blohm, M. *Appl. Phys. Lett.* **2009**, *94*, 133109.

[36] Lembach, A. N.; Tan, H.-B.; Roisman, I. V.; Gambaryan-Roisman, T.; Zhang, Y.; Tropea, C.; Yarin, A. L. *Langmuir* **2010**, *26*, 9516.

[37] Tsai, P.; van der Veen, R. C. A.; van de Raa, M.; Lohse, D. *Langmuir* **2010**, *26*, 16090.

[38] Rioboo, R.; Voué, M.; Vaillant, A.; De Coninck, J. *Langmuir* **2008**, *24*, 14074.

[39] Jung, Y. C.; Bhushan, B. *Langmuir* **2009**, *25*, 9208.

[40] Xu L.; Barcos L.; Nagel S. R. *Phys. Rev. E* **2007**, *76*, 066311.

[41] Reyssat, M.; Richard, D.; Clanet, C.; Quere, D. *Faraday Discussions* **2010**, *146*, 19.

[42] Apel-Paz, M.; Marmur, A. *Colloid Surface A* **1999**, *146*, 273.

[43] Woodward, I. S.; Schofield, W. C. E.; Roucoules, V.; Badyal, J. P. S. *Langmuir* **2003**, *19*, 3432.

[44] Woodward, I. S.; Schofield, W. C. E.; Roucoules, V.; Badyal, J. P. S. *Plasma Chem. Plasma Process.* **2006**, *26*, 507.

[45] Evans, J. F.; Gibson, J. H.; Moulder, J. F.; Hammond, J. S.; Goretzki, H. Fresenius J. *Anal. Chem*. **1984**, *841*, 319.

[46] Bridgman, P. W. *Dimensional Analysis*; Yale University Press: New Haven, 1931.

[47] Schiaffino, S.; Sonin, A. A. *Phys. Fluids* **1997**, *9*, 3172.

[48] Pasandideh-Fard, M.; Qiao, Y. M.; Chandra, S.; Mostaghimi, J. *Phys. Fluids* **1996**, *8*, 650.

[49] Attané, P.; Girard, F.; Morin, V. *Phys. Fluids* **2007**, *19*, 012101.

[50] van Dam, D. B.; Le Clerc, C. *Phys. Fluids* **2004**, *16*, 3403.

[51] Hopkins, J.; Badyal, J. P. S. *J. Phys. Chem.* **1995**, *99*, 4261.

[52] Brown, W. R.; Jenkins, R. B.; Park, G. S. *J. Polym. Sci. Pol. Sym.* **1973**, *41*, 45.

[53] Youngblood, J. P.; McCarthy, T. J. *Langmuir* **1999**, *32*, 6800.

[54] Olde Riekerink, M. B.; Terlingen, J. G. A.; Engbers, G. H. M.; Feijen, J. *Langmuir* **1999**, *15*, 4847.

[55] Kim, K. S.; Ryu, C. M.; Park, C. S.; Sur, G. S.; Park, C. E. *Polymer* **2003**, *44*, 6287.

[56] Murase, H.; Fujibayashi, T. *Prog. Org. Coat.* **1997**, *31*, 97.

[57] Miwa, M.; Nakajima, A.; Fujishima, A.; Hashimoto, K.; Watanabe, T. *Langmuir* **2000**, *16*, 5754.

[58] Öner, D.; McCarthy, T. J. *Langmuir* **2000**, *16*, 7777.

[59] Strani, M.; Sabetta, F. *J. Fluid Mech.* **1984**, *141*, 233.

[60] Strani, M.; Sabetta, F. *J Fluid Mech.* **1988**, *189*, 397.

[61] Fetzer, R.; Ralston, J. *J. Phys. Chem. C* **2010**, *114*, 12675.

[62] Kannangara, D.; Shen, W. *Colloids Surf., A* **2008**, *330*, 151.

[63] Gao, L.; McCarthy, T. J. *Langmuir* **2006**, *22*, 2966.

[64] Castrejon-Pita, J. R.; Betton, K. J.; Kubiak, K. J.; Wilson, M. C. T.; Hutchings, I. M. *Biomicrofluidics* **2011**, *5*, 014112.